



LAWRENCE
LIVERMORE
NATIONAL
LABORATORY

Morphological Design of Silicon Electrode with Anisotropic Interface Reaction Rate for Lithium Ion Batteries

Y. An, B. C. Wood, Y. M. Wang, M. Tang, H.
Jiang

October 23, 2014

Physical Chemistry Chemical Physics

Disclaimer

This document was prepared as an account of work sponsored by an agency of the United States government. Neither the United States government nor Lawrence Livermore National Security, LLC, nor any of their employees makes any warranty, expressed or implied, or assumes any legal liability or responsibility for the accuracy, completeness, or usefulness of any information, apparatus, product, or process disclosed, or represents that its use would not infringe privately owned rights. Reference herein to any specific commercial product, process, or service by trade name, trademark, manufacturer, or otherwise does not necessarily constitute or imply its endorsement, recommendation, or favoring by the United States government or Lawrence Livermore National Security, LLC. The views and opinions of authors expressed herein do not necessarily state or reflect those of the United States government or Lawrence Livermore National Security, LLC, and shall not be used for advertising or product endorsement purposes.

Morphological Design of Silicon Electrode with Anisotropic Interface Reaction Rate for Lithium Ion Batteries

Yonghao An^{1,2}, Brandon C. Wood², Yinmin Morris Wang², Ming Tang^{*3}, Hanqing Jiang^{*1}

¹School for Engineering of Matter, Transport and Energy, Arizona State University, Tempe, AZ 85286, USA

²Physical and Life Sciences Directorate, Lawrence Livermore National Laboratory, Livermore, CA 94550, USA

³Department of Materials Science and NanoEngineering, Rice University, Houston, TX 77005

Abstract

Silicon is one of the most promising materials for high-capacity electrodes in next-generation lithium (Li) ion batteries. However, it presents significant engineering challenges, since the initial lithiation of crystalline silicon involves huge volume expansion, plastic flow of material, and electrochemically induced amorphization that can collectively lead to mechanical failure. We propose a new principle for the geometric design of a silicon electrode that leverages the anisotropic orientation dependence of the interface velocity to mitigate internal stresses that result from plastic deformation, allowing us to specify optimal geometries for nanoparticles and nanowires of common orientations. The principle is informed and validated by the development of a coherent anisotropic three-dimensional solid reaction model that imposes crystallographic symmetry constraints, and has the advantage of describing the orientation-dependent interface velocity in terms of physically motivated quantities that may be directly obtained from experiments or first-principles calculations. In addition to reproducing known morphologies of both silicon nanowires and nanoparticles upon lithiation, the continuum model reveals the formation of a faceted crystal core and plastic necking along particular directions, which we correlate directly to experimental observations of fracture to motivate our design strategy.

Introduction

The rapidly increasing demand for widespread applications of lithium (Li) ion batteries (LIBs) in portable electronics, electric/hybrid vehicles, and smart-grid storage for green energy, calls for the development of electrode materials with significantly improved energy density, rate capability and life span¹⁻³. Silicon (Si) as a Li-alloying anode has attracted enormous interest in recent years⁴⁻⁶ due to its very high specific capacity (4000mAh/g). Lithium insertion into crystalline silicon results in a transformation to an amorphous Li_xSi alloy, which is accompanied by very large volume expansion of >300%. Such a huge volume change generates significant stress and causes the pulverization of large silicon particles upon the first cycle of lithiation, as well as rapid capacity fading. To overcome the problem of Li-insertion-induced mechanical failure, various approaches to tailoring Si electrode structures have been explored¹¹, such as improving the interaction between Si and other electrode components¹², and employing silicon nanowires and nanoparticles¹³. Downscaling silicon structures to the nano regime allows the internal stress to be effectively relieved upon (de)lithiation, which substantially enhances capacity retention. Nevertheless, crack initiation and growth during lithium insertion and extraction remains a significant impediment even in silicon nanostructures [14]; for example, Lee *et al.* found that more than 90% of <111> axially oriented crystalline Si nanopillars with diameters of 300-400 nm fractured upon first lithiation [16].

A significant finding from recent experiments is that the volume change of crystalline silicon nanostructures upon Li insertion is highly anisotropic. Liu *et al.* discovered that <112>-oriented silicon nanowires with an initially circular cross-section evolve into a dumbbell shape after lithiation [14]. Lee *et al.* found that electrochemical lithium insertion causes round silicon nanopillars with <100>, <110> and <111> axial orientations to expand into anisotropic shapes with 4-, 2- and 6-fold symmetry, respectively [15]. A common feature observed among nanowires of different orientations is that they swell most significantly along the <110> direction and least in the <111> direction, with the <100> and <112> directions in between. To understand the origin of this anisotropic shape change, Liu *et al.* performed *in*

situ transmission electron microscopy (TEM) to characterize the evolution of the growth front of amorphous Li_xSi in individual Si nanowires during lithium insertion with atomic resolution [19]. They observed that the amorphous Li_xSi alloy and crystalline Si regions form a sharp interface, which migrates through the movement of steps on close-packed $\langle 111 \rangle$ atomic planes. This migration mechanism results in an orientation-dependent interface velocity (or reaction rate), which is lowest in the $\langle 111 \rangle$ direction and much higher along $\langle 110 \rangle$, and is responsible for the development in the shape anisotropy of nanowires/pillars.

The anisotropic swelling behavior has important implications for the chemomechanical stability of silicon nanostructures as LIB anodes. It is observed that upon first lithiation, fracture initiates on the sidewall surface of crystalline Si nanopillars predominantly along the slow-swelling directions [16], e.g. $\langle 100 \rangle$ for pillars with $\langle 110 \rangle$ axial orientation and $\langle 112 \rangle$ for pillars with $\langle 111 \rangle$ axis. These cracks grow and become more severe with subsequent electrochemical cycling, and can eventually cause splitting of an entire pillar. The preferential orientations of crack formation are explained on the basis that the $\langle 110 \rangle$ -oriented fast volume expansion leads to tensile hoop stress concentration and hence fracture on pillar surface in the slower swelling directions [16, 18]. Lithiation-induced cracks can not only cause increase in impedance and even loss of contact between active material and current collector, but they also expose more silicon to the surrounding electrolyte in the battery. This leads to the formation of more unwanted side reaction products that contribute to the solid-electrolyte interphase (SEI), which in turn decreases the reversible capacity. In this way, the anisotropic shape change of silicon structures directly facilitates electrode degradation and is detrimental to battery performance.

As shown by Lee *et al.* [16], size reduction of silicon structures below a critical dimension (e.g. ~ 200 nm for $\langle 111 \rangle$ pillars) could effectively suppress (de)lithiation-induced fracture. Nonetheless, this approach also has a significant disadvantage in generating a large surface-to-volume ratio, which accelerates capacity fade due to SEI formation on electrode surfaces and reduces the packing density of the active material. In this paper, we propose a different strategy to mitigate fracture in silicon anodes

through rational design of the pristine silicon anode morphology. The central idea underlying our approach is to promote a much more uniform swelling of the electrode by deliberately engineering the shape of the Si electrode so as to compensate for the anisotropic volume expansion. A more isotropic electrode swelling helps avoid tensile stress or strain concentration in the amorphous phase and suppress crack initiation. We demonstrate the effectiveness of our design for both nanopillars and nanoparticles through a new mesoscale model described below.

Model

The anisotropic expansion of lithiated silicon nano-wires or pillars has been studied by several continuum models. In Ref. 14, lithiation-induced strain in Li_xSi alloys is assumed to be anisotropic to explain the dumbbell shape of a $\langle 112 \rangle$ -orientated nanowire. In Ref. 18, anisotropic diffusivity of Li is assigned in the interfacial region between crystalline Si and amorphous Li_xSi to numerically produce an orientation-dependent interface velocity. While these models successfully reproduce experimentally observed Si morphologies, their predictive power is limited by several factors. First, they introduce anisotropy through *ad hoc* approaches that are not entirely consistent with the experimental finding that the anisotropic behavior primarily originates from the interface reaction kinetics at the crystalline/amorphous phase boundary. Second, it is not easy to unequivocally determine the values of adjustable parameters in these models based on inputs that can be directly measured from experiment or calculated using atomistic models (such as the interface velocity or reaction rate), making quantitative simulation challenging. For these reasons, a new interface reaction model is employed here.

In our model, the phase boundary between silicon (c-Si) and amorphous Li_xSi alloy (*a*- Li_xSi) is treated as a sharp interface of zero thickness, which advances at a given velocity $v(\mathbf{n})$ that is a function of interface orientation. At the interface, c-Si is transformed into *a*- Li_xSi through the solid-state chemical reaction $x\text{Li}^+ + xe^- + \text{Si} \rightarrow \text{Li}_x\text{Si}$. The interface velocity is proportional to the rate of the interfacial chemical reaction R_s . According to the theory of chemical reaction kinetics, $R_s = k[\text{Li}^+]^x[\text{e}^-]^x[\text{Si}]/$

$[Li_xSi]$ [unit: mole/(area•time)], where k is the rate constant, and $[Li^+]$, $[e^-]$ and $[Si]$ represent the concentrations of all reactants (Li ions, electrons and silicon) at the interface. We note that the concentrations of Li^+ and e^- at the reaction front (and hence the interface velocity) are influenced not only by the interfacial reaction kinetics but also by the rate of lithium diffusion through the α - Li_xSi shell upon lithiation, which is a bulk process. However, Li diffusion kinetics becomes increasingly facile with decreasing electrode dimensions, causing its effect on $[Li^+]$ and $[e^-]$ to diminish. The critical feature size of an electrode below which Li diffusion has negligible influence on the interface velocity v can be estimated as $a_c = D/v$, where D is the Li diffusivity. Using representative values^{19, 29, 30}

$D = 1 \times 10^{-12} \text{ cm}^2 / \text{s}$ and $v_{\text{max}} = 5 \text{ nm} / \text{min}$, we obtain $a_c = 1 \mu\text{m}$. Therefore, for nanoscale Si anode structures it is a reasonable approximation to treat the concentrations of all reactants at the interface as constants that do not vary with time or interface orientation. The interface velocity $v(\mathbf{n})$ is thus set as a time-independent function of the interface orientation in our model; its anisotropy exclusively reflects that of the reaction constant k , which is a materials property.

The function form of $v(\mathbf{n})$ is constrained by the fact that it must conform to the cubic symmetry of c-Si, i.e., $v(\mathbf{n})$ must be unchanged by symmetry operations of the Si crystal structure. There exist various methods^{31,32} to construct expressions that satisfy the symmetry requirement. Here we use the invariant theory^{33, 34} to expand $v(\mathbf{n})$ as $v(\mathbf{n}) = A_1 I_1 + A_2 I_2 + A_3 I_3 + A_4 I_2^2 + \dots$, where $I_k(\mathbf{n})$ ($k=1,2,3,\dots$) are polynomials of increasing degrees of invariance with respect to cubic symmetry operations. The expressions for I_1 , I_2 and I_3 and their values in several directions of interest are given in Table 1. The level surfaces of I_1 , I_2 and I_3 are plotted in Fig. S2a. We truncate the polynomial series at I_2^2 to make $v(\mathbf{n})$ tractable for simulations. The coefficients A_k ($k=1-4$) control the anisotropy of $v(\mathbf{n})$, and their values could in principle be directly determined from interface velocity data through experimental measurements or atomistic modeling. Though such data are still scarce, the *in situ* TEM experiment of lithiation of c-Si nanowires by Liu *et al.* [19] provides two important observations, i.e., the interface velocity along $\langle 111 \rangle$

directions is vanishingly small, whereas $\{110\}$ facets exhibit the highest velocity among the observed interface orientations. Based on these findings, we impose the following requirements on the low-index orientations of $v(\mathbf{n})$:

- 1) The $\{111\}$ interface has zero velocity: $v_{\langle 111 \rangle} = 0$.
- 2) Interface velocity reaches a global maximum in the $\langle 110 \rangle$ direction: $v_{\langle 110 \rangle} = v_{\max}$.
- 3) The velocity of $\{100\}$ is η ($0 < \eta < 1$) times of that of $\{110\}$: $v_{\langle 100 \rangle} = \eta v_{\max}$.

The same ordering is employed in a previous continuum modeling study [18]. A functional form that

satisfies the above requirements is $v = v_{\max} \left(1 - 16(1-\eta) \left(I_2 - \frac{1}{4} \right)^2 - 3(8+\eta)I_3 \right)$, where η is an

adjustable parameter that controls the anisotropy of $v(\mathbf{n})$. This expression for $v(\mathbf{n})$ is used in all simulations in this paper.

Given the lack of experimental or modeling data offering precise interface reaction velocities for all low-index facets, the exact value of η is difficult to ascertain. However, we found that the simulation results are rather insensitive to η , provided that the qualitative ordering of the interface velocities in $\langle 110 \rangle$, $\langle 100 \rangle$, and $\langle 111 \rangle$ remains unchanged (see Supplementary Information, Figure S6). Nevertheless, to provide some physical motivation for our choice of η , it is desirable to extract interface reaction kinetics directly from atomistic descriptions. We point out that other groups have previously employed dynamical frameworks based on first-principles density functional theory (DFT) calculations to extract Li reaction kinetics at Si surfaces, but the results do not permit full parameterization of η . For instance, Cubuk *et al.* used a multiscale model based on DFT and kinetic Monte Carlo to confirm that the (111) surface shows slower lithiation reaction kinetics than the (110) surface, but other facets with intermediate reaction kinetics were not explored [20]. On the other hand, Chan *et al.* considered the (100) surface in addition to (110) and (111) using first-principles molecular dynamics, but the relative ordering of the reaction barriers was found to depend nontrivially on Li surface concentration (and by extension, the

surface flux), making comparison with observations of interface velocities difficult [27]. In the absence of a truly dynamical description of the reaction kinetics at each facet, we avoid such complexities by instead comparing the elastic response of (100), (111), and (110) facets, calculated using DFT. Specifically, we compute the dependence of the surface energy on local Si tensile and compressive surface strain, which is related to the surface tension (see Supplementary Information). Surface reconstruction is not considered in the calculations, since there is no evidence that reconstruction will occur at the reaction front with lithiated α -Si, where ion mobility and entropy are high, and ions are freely available to passivate dangling bonds and equilibrate local potentials. Although not as sophisticated as the treatments in Refs 27 and 20, our method should provide a reasonable indication of the difference in Li insertion barriers and hence reaction kinetics on various facets because it reflects the ease (or difficulty) of the expansion or contraction of individual Si-Si bonds upon Li insertion. The calculation confirms that the (100) surface accommodates lattice strain much more poorly than (110), with (111) even poorer (see Figure S7). Based on this input, we conclude that the interface velocities should order as $(110) \gg (100) > (111)$, i.e. $\eta \ll 0.5$. Consistent with this finding, $\eta=1/6$ is used throughout this paper. The interface velocity at this η value is plotted as a function of interface orientation in Fig. S2e.

In our numerical simulation of the lithiation process in c-Si nanopillars (2D) and nanoparticles (3D), the position of the interface between c-Si and α -Li_xSi is updated at every time step according to $v(\mathbf{n})$, using a robust front tracking method described in the “Method” section, which is very efficient for simulating the evolution of convex shapes. Because the dimensions of the nanostructures are small relative to the characteristic lengthscales associated with the Li diffusion process, the normalized Li concentration in the amorphous phase is assumed to be saturated at all times, i.e. $\bar{c} = c / c_{\max} = 1$, where c_{\max} is the maximal lithium concentration in α -Li_xSi. On the other hand, $\bar{c} = 0$ is assigned to the c-Si core because of the very small solubility of Li in crystalline silicon. Therefore, the Li concentration in the anode is updated in the simulation without solving the diffusion equation. The deformation and mechanical constitution of the electrode is described using large deformation theory (a detailed discussion

can be found in our previous work²³). The lithiation-induced volume expansion is assumed to be linearly dependent on Li concentration, as $\left. \frac{V}{V_0} \right|_{\bar{c}} = 1 + \lambda \bar{c}$. Similar to previous works³⁹⁻⁴¹, c-Si is modeled as a linear elastic material with Young's modulus $E_c = 130 \text{ GPa}$ and Poisson's ratio $\nu = 0.28$, and a-Li_xSi is modeled as perfect elastic-plastic material with $E_a = 12 \text{ GPa}$, $\nu = 0.28$ and yield stress $Y = 0.5 \text{ GPa}$. These values are taken from the literature^{39, 42, 43}. The simulation is implemented in the commercial finite element package ABAQUS. More detailed implementation information is provided in the “Method” section.

Results and Discussion

Lithiation of c-Si nanopillars with an initially circular cross-section

We first study the initial lithiation of crystal Si nanowires with circular cross-sections. Four nanowires with radius $a = 100 \text{ nm}$ oriented along $\langle 100 \rangle$, $\langle 110 \rangle$, $\langle 111 \rangle$, and $\langle 112 \rangle$ directions are studied. A plane strain condition is applied in the axial direction for simplicity. As an example, the results for $\langle 112 \rangle$ nanowire are shown in Figure 1, with results for the other nanowire configurations presented in Fig. S3. Fig. 1a shows the normalized velocity of the amorphous-crystalline interface (ACI), $r = v(\theta) / v_{\max}$, as a function of orientation θ in $\{112\}$ plane. The velocity plot exhibits a butterfly shape, which has a global maximum in $\langle 110 \rangle$ direction, a second maximum at about 55° away from $\langle 110 \rangle$ that correspond to crystallographic direction $\langle 13 \ 1 \ 7 \rangle$, and a minimum in $\langle 111 \rangle$ direction. We refer to $\langle 110 \rangle$ and $\langle 13 \ 1 \ 7 \rangle$ as the primary and secondary ACI directions in the description below. As shown in Figure 1(b) and Figure S3(d), as lithiation proceeds, the fastest-moving $\{110\}$ and $\{13 \ 1 \ 7\}$ planes gradually become the dominant orientations of the ACI. The other orientations are eventually eliminated from the ACI, resulting in a faceted c-Si core. As indicated by the colormap of maximal in-plane stress in the wire cross-section plane at normalized time $\tau = t v_{\max} / a = 0.2$ (Fig. 1c), the crystal core is always subjected to tensile stress upon first lithiation due to lithiation-induced expansion along the ACI (white

line). In contrast, the stress state of the amorphous shell has two distinct regions — the stress is compressive in the region immediately behind the moving ACI (in dark blue), but switches to tension further away from the ACI. The change in the stress character from compression to tension is caused by the geometric constraints that are active at the ACI. Whenever a thin crystalline material layer is swept into the ACI, it undergoes a volume expansion due to the crystalline-to-amorphous phase transformation. However, this expansion is constrained by the c-Si core and the outer amorphous layer which has already deformed plastically. Therefore the thin amorphous layer immediately behind the ACI is compressed in the hoop direction, while the crystalline core and the outer amorphous layer are under tension. Because the crystalline-to-amorphous transformation has the largest reaction rates along $\langle 110 \rangle$ and $\langle 1\bar{1}1 \rangle$, the $a\text{-Li}_x\text{Si}$ shell expands most significantly in these two directions. In contrast, swelling is smaller along $\langle 111 \rangle$ due to the minimal ACI velocity in this direction. Furthermore, material near the nanowire surface is driven by tensile stress to flow plastically from $\langle 111 \rangle$ towards the primary and secondary ACI directions. Constrained by the volume conservation associated with plastic deformation, such material flow in the hoop direction induces necking around $\langle 111 \rangle$, and further thins down the $a\text{-Li}_x\text{Si}$ shell thickness in this direction. As illustrated by the colormap of the equivalent plastic strain (PEEQ) on the nanowire surface at $\tau = 0.2, 0.4$, and 0.6 in Fig. 1b, the plastic necking generates highly concentrated plastic strain in the outermost amorphous shell near the $\langle 111 \rangle$ orientation, which can lead to the initiation of surface cracks as discussed below. The dumbbell shape of the lithiated $\langle 112 \rangle$ nanowire obtained by our simulation agrees qualitatively with the TEM observation by Liu *et al.* [14] (Figure 1(d)) and the simulation by Yang *et al.* [18].

The simulated morphological evolution of nanowires with $\langle 001 \rangle$, $\langle 110 \rangle$ and $\langle 111 \rangle$ axial orientations upon lithiation is shown in Fig. S3a-c. The main features seen in the simulation of the $\langle 112 \rangle$ nanowire, i.e. the formation of faceted c-Si cores, anisotropic shape change of the $a\text{-Li}_x\text{Si}$ shell, and plastic necking in certain directions, are also observed in these cases. The good agreement between our

simulated lithiated nanowire shapes in Fig. S3 and available results from experiments¹⁵ and a different modeling method [18] for various nanowire orientations supports the validity of our simulation approach.

Lithiation of c-Si nanoparticles with an initially spherical shape

After examining the shape evolution of nanowires in 2D, we extended the study to the lithiation of nanoparticles in 3D simulation. As is seen from Figure 2a, the ACI velocity in the 3D orientation space has global minima along $\langle 111 \rangle$ directions, local minima along $\langle 100 \rangle$, and global maxima along $\langle 110 \rangle$. The morphological evolution of an initially spherical particle with a radius $a=100$ nm upon lithiation is shown in Figure 2(b). As lithiation proceeds, the nanoparticle expands anisotropically, forming “hills” in $\langle 110 \rangle$ directions and “valleys” in $\langle 100 \rangle$ and $\langle 111 \rangle$ directions. As illustrated by the colormap superimposed on the particle surface in Figure 2(b), the PEEQ distribution at the outermost amorphous shell shows an interesting evolution with time: at early stages (e.g., at $\tau = 0.1$) PEEQ is the largest in $\langle 110 \rangle$ directions, whereas plastic deformation becomes most severe near $\{100\}$ planes at later stages ($\tau = 1$). Figure 2(c) presents the snapshots of the crystalline core of the nanoparticle at different times. Similar to 2D nanowires, the fastest-moving crystallographic planes become increasingly dominant at the ACI as the c-Si core shrinks, until the core eventually becomes a rhombic dodecahedron bounded by $\{110\}$ facets. As shown in Figure 2(d), the (111) cross-section of the particle at an intermediate simulation time is remarkably similar to the TEM image of a partially lithiated spherical Si nanoparticle found in the literature⁴⁴. To our knowledge, this is the first time that the experimentally observed Si nanoparticle morphology during lithiation is faithfully captured by modeling.

Morphological design of Si nanowire & nanoparticle anodes

Fracture or mechanical degradation of Si anodes in LIB upon electrochemical cycling is widely studied as a major factor that adversely affects LIB performance. In Fig. 3, TEM images from the literature [14,16] that show the directional fracture of $\langle 100 \rangle$ and $\langle 112 \rangle$ Si nanowires are compared against the PEEQ color maps of partially lithiated nanowires computed at representative times. It is seen

that the locations of cracks on the nanowires coincide with the plastic strain concentration regions in the amorphous phase, which clearly points out that lithiation-induced plastic necking instability of nanowires is responsible for crack initiation and growth.

Here we demonstrate that it is possible to mitigate the catastrophic plastic flow and hence improve fracture performance through the use of Si nanowires with anisotropic cross-section shapes. Note that this idea differs from previous improvement strategies for silicon anodes, which have mainly relied on decreasing nanostructure size to enhance fracture resistance. Our strategy is inspired by the observation that highly concentrated tensile strain near the surface of the amorphous shell is generated by the anisotropic volume expansion of nanowires upon lithium insertion. When starting from a circular cross-section, a nanowire swells the least in the slow ACI moving direction (e.g. $\langle 100 \rangle$ for $\{001\}$ nanowires and $\langle 111 \rangle$ for $\{112\}$ nanowires). The non-uniform swelling results in plastic flow from the slow to fast ACI directions on the nanowire surface, which induces necking instability in the slow ACI direction. However, by making the cross-section of Si nanowires non-circular, the anisotropy in the ACI motion can be compensated by an anisotropic nanowire morphology that is deliberately engineered to produce a more isotropic expansion. This should reduce localized strain concentration at nanowire surface regions that serve as crack initiation sites, thereby improving nanowire stability under lithiation.

Upon exploring promising designs of nanowire morphology that could help mitigate fracture, we observe that regardless of its initial shape, the shape of the c-Si core eventually converges upon lithiation to a polygonal object that is surrounded by ACI planes of the highest growth velocities. Intuitively, using a similar polygon geometry as the initial cross-section of nanowires could offer distinctive benefits. Such nanowires would have smaller dimensions in the fast-moving ACI directions (i.e. along the polygon side normals) than in the slow ACI directions, which point towards polygon vertices. This directional size difference should offset the larger swelling in the fast ACI directions and promote isotropic expansion. In addition, the ACI will retain its faceted morphology throughout the Li insertion process, which should improve the stability of the nanowire morphology and prevent any dramatic shape change that could

enhance local strain/stress concentration. For $\langle 100 \rangle$ and $\langle 111 \rangle$ nanowires, the proposed cross-sections are a simple square and regular hexagon with $\{110\}$ sides, respectively, as shown in Figure S3. For $\{112\}$ and $\{110\}$ nanowires, however, the polygons consist of two families of crystallographic planes, i.e. primary and secondary ACI directions, that correspond to the largest and second largest local maxima of the ACI velocity (Figures 1 and S3). To ensure that the ACI morphology remains self-similar during evolution, we further require the nanowire dimensions in the primary and secondary directions to scale with their ACI velocities. Therefore, our proposed design of initial nanowire cross-section is *a polygon that satisfies two conditions: 1) its sides are perpendicular to the primary ACI directions (and also secondary directions if necessary); and 2) the distance from each side to the center is proportional to the ACI velocity along its normal.*

The effectiveness of our design concept is validated by simulations. As an example, Figure 4(a) shows the tailored cross-section shape of a $\langle 112 \rangle$ nanowire, which is bounded by two $\{110\}$ planes and four $\{13\bar{1}7\}$ planes that are 55° apart from $\{110\}$. The distances between the two types of sides to the polygon center are $a=100\text{nm}$ and $l=0.91a$, respectively. As is seen from the snapshots in Figure 4(b), the initial polygon shape of c-Si counteracts the anisotropic swelling of the amorphous phase and lets the nanowire achieve a much more isotropic morphology than the original circular nanowire (cf. Figure 1(b)) at normalized lithiation time $\tau=0.2$. Upon further lithiation the aspect ratio of the circular nanowire becomes much larger at $\tau=0.4$ and 0.6 , but the cross-section of the designed nanowire remains approximately circular. The isotropy of the nanowire's cross-section can be quantitatively characterized by the two-dimensional circularity parameter, defined as $C = 2\sqrt{\pi A} / L$, where A and L are the area and perimeter of the cross-section, respectively, and C attains its maximum of 1 for a circle. The circularity values of polygon-shaped and circular $\{112\}$ nanowires as a function of lithiation time are compared in Figure 4(c). While the circular nanowire exhibits continuous decrease in C , the circularity of the polygon-shaped nanowire increases initially because of the transition from polygon to circular cross-section and then maintains a value very close to 1 until the completion of lithiation. The more isotropic expansion of

the {112} nanowire contributes to the significant reduction of strain concentration. Comparing Figure 1(b) and 4(b), it is evident that the magnitude of PEEQ in the amorphous shell is substantially lower at any time of lithiation when the initial cross-section changes from circle to polygon. Figure 4(d) presents the angular distribution of PEEQ on the nanowire surface at $\tau=0.3$ for both circular and polygonal cross-sections. The highly concentrated plastic strain in the $\langle 111 \rangle$ slow lithiation direction that triggers crack growth is no longer seen in the polygon-shaped nanowire. The largest PEEQ instead occurs along the fast ACI moving direction $\langle 110 \rangle$, but the strain concentration is much less severe than in the case of circular nanowire and no necking instability develops along $\langle 110 \rangle$ during Li insertion, thanks in part to the large thickness of the amorphous shell in this direction. The simulation results for $\langle 100 \rangle$, $\langle 110 \rangle$ and $\langle 111 \rangle$ -oriented nanowires with polygon cross-sections are compared against the case of circular nanowires in Figures S4 and S5. Similar improvements are observed upon introduction of the anisotropic nanowire morphology design, the only exception being the $\langle 111 \rangle$ nanowire, which has only a weakly anisotropic ACI velocity profile within its cross-section.

Using a similar strategy, a rhombic dodecahedron geometry is proposed for a Si electrode particle to mitigate fracture, with all its twelve faces orientated in $\langle 110 \rangle$ directions as illustrated in Figure 5(a). This design is identical to the convergent shape of the shrinking crystalline core during lithiation, as seen in Figure 2(c). As shown in Figure 5, after Li insertion starts, the polyhedral particle quickly obtains an approximately spherical shape with fast growth in $\langle 110 \rangle$ directions, with only small “dents” or “ridges” present at polyhedron edges and vertices. Similar to the 2D case, the isotropy of the electrode particle can be quantitatively measured by the sphericity parameter, defined as $S = 2(6\pi^2V)^{1/3} / A$, where V and A are particle volume and surface area, respectively, and a sphere has a maximal S value of 1. The comparison between the sphericity values of the particles with originally polyhedral and spherical shapes upon lithiation in Figure 5(b) clearly shows that the polyhedral design is superior in achieving a highly isotropic particle expansion. As a result, the PEEQ value is much lower and more uniformly distributed on the particle surface (Figure 5(a)) than in a spherical particle (Figure 2(a)).

Though the simulations presented above use nanowires and nanoparticles as examples, our results are in principle size independent, and are therefore also applicable to electrodes of larger dimensions. Our design concept could be easily implemented for micro-sized silicon structures such as micropillars, for which anisotropic cross-section shapes can be fabricated through conventional photolithography techniques. Electrodes with smaller feature sizes could be achieved via direct growth⁴⁶ or controlled anisotropic etching of silicon wafers/particles as suggested in literature⁴⁷⁻⁴⁹. By extending the approach to larger, micro-sized silicon electrodes, one could avoid issues arising from the large surface area of nanostructures, which tends to increase SEI formation rate and lower the packing density of the active ingredient, adversely affecting the electrode's energy density. Furthermore, it should be emphasized that the benefit of our design extends beyond the first lithiation cycle. Experiments show that silicon anodes remain in the amorphous phase during electrochemical cycling after initial discharge. As ion/electrode diffusion is typically isotropic in amorphous structures, the highly isotropic electrode morphology produced by the first lithiation of anisotropically shaped silicon structures will promote a uniform strain/stress distribution within the electrode and thus reduce the risk of fracture in subsequent charge/discharge cycles. In addition, the lower surface-to-volume ratio associated with isotropic 2D or 3D electrode structures will help to decrease interface side reaction rates and improve capacity retention.

Conclusion

In conclusion, we establish a new polygon/polyhedron design paradigm for silicon electrodes, which leverages the intrinsic anisotropy of interface reaction fronts in crystalline silicon so as to directly mitigate internal stresses and strains associated with lithiation. The proposed structures should demonstrate short- and long-term mechanical integrity, as well as improved rate performance. The viability of the design rule is confirmed through the development and application of a new continuum model for reaction-controlled interface migration in crystalline silicon, which incorporates information from experiments and atomistic calculations, as well as crystallographic symmetry considerations. When applied to silicon electrodes composed of circular cross-section nanowires or spherical nanoparticles, it

successfully captures the experimentally reported morphology evolution and reaction kinetics. It further depicts the formation of a faceted crystal core and predicts plastic instability, which we are able correlate with the buildup of internal stresses associated with fracture. Our new model offers several additional advantages. First, the theoretical formulation and numerical implementation are self-consistent and general, and can be readily applied to structures with any two/three dimensional geometry. Second, all of the model parameters have clear physical significance, and are in principle directly measurable. Third, the model can be easily extended within the same numerical implementation as more detailed information on the ACI velocities becomes available, either from experiments or atomic calculations.

Funding was provided by LLNL LDRD Grant 12-ERD-053. A portion of this work was performed under the auspices of the U.S. Department of Energy by LLNL under Contract DE-AC52-07NA27344.

Method

A front tracking method is used to calculate the evolution of the ACI, which is exclusively determined by the initial geometry of the electrode (i.e., the initial position of the ACI), and the velocity of the ACI as a function of orientation. The algorithm for this front tracking method is illustrated in [Fig. S1b](#) for the 2D calculation (see Supporting Information). The initial position of the ACI, or equivalently, the original boundary of the *c*-Si electrode, is described by a curve (for 2D) or curved surface (for 3D). The initial ACI is discretized by a set of points with equal separation, and the tangent line or plane of the ACI at each of these points is determined. A fine mesh is used to discretize the initial configuration of the ACI in order to ensure very small shifts in orientation between adjacent tangent lines or planes and preserve accuracy. For the analysis described in this letter, 360 points are used for 2D, and 360×180 points for 3D. Each tangent line or plane has a unique normal direction pointing toward the inside of the envelope. At every time step during lithiation, the positions of all the tangent lines or planes are updated according to the ACI velocity $v(n)$ in the corresponding tangent normal direction as defined in the “Model” section. Subsequently, the ACI at the new time is determined by the smallest envelope formed by the tangent lines or planes. After updating the ACI position, the normalized Li concentration $\bar{c} = 0$ is

assigned inside the envelope for the c -Si phase, and $\bar{c} = 1$ outside for a -Li_xSi. A smooth transition of c is applied to a very thin layer across the ACI to facilitate numerical convergence. The above described algorithm is implemented in ABAQUS user subroutine UTEMP. Another user subroutine UEXPAN is employed to specify the stress-free strain due to lithiation-induced volumetric expansion in a -Li_xSi in a way consistent with a total Lagrangian description for large deformation (see detailed discussion in our previous work²³). c -Si is modeled as linear elastic material, and a -Li_xSi as perfect elastic-plastic material. Material properties are interpolated between c -Si and a -Li_xSi in the thin transition region across ACI where \bar{c} varies. The mechanical constitution is implemented by ABAQUS built-in modules for the concentration-dependent properties. The implicit plastic-elastic solver in ABAQUS/Standard is employed, with the nonlinear geometry option enabled for large deformation problems.

References

1. Armand, M.; Tarascon, J. M., Building better batteries. *Nature* 2008, 451, 652-657.
2. Tarascon, J. M.; Armand, M., Issues and challenges facing rechargeable lithium batteries. *Nature* 2001, 414, 359-367.
3. Arico, A. S.; Bruce, P.; Scrosati, B.; Tarascon, J. M.; Van Schalkwijk, W., Nanostructured materials for advanced energy conversion and storage devices. *Nature Materials* 2005, 4, 366-377.
4. Wu, H.; Chan, G.; Choi, J. W.; Ryu, I.; Yao, Y.; McDowell, M. T.; Lee, S. W.; Jackson, A.; Yang, Y.; Hu, L. B.; Cui, Y., Stable cycling of double-walled silicon nanotube battery anodes through solid-electrolyte interphase control. *Nat Nanotechnol* 2012, 7, 309-314.
5. Chan, C. K.; Peng, H. L.; Liu, G.; McIlwrath, K.; Zhang, X. F.; Huggins, R. A.; Cui, Y., High-performance lithium battery anodes using silicon nanowires. *Nat Nanotechnol* 2008, 3, 31-35.
6. Magasinski, A.; Dixon, P.; Hertzberg, B.; Kvit, A.; Ayala, J.; Yushin, G., High-performance lithium-ion anodes using a hierarchical bottom-up approach. *Nature Materials* 2010, 9, 353-358.
7. Winter, M.; Besenhard, J. O.; Spahr, M. E.; Novak, P., Insertion electrode materials for rechargeable lithium batteries. *Advanced Materials* 1998, 10, 725-763.
8. Chung, S. Y.; Bloking, J. T.; Chiang, Y. M., Electronically conductive phospho-olivines as lithium storage electrodes. *Nature Materials* 2002, 1, 123-128.
9. Dahn, J. R.; Zheng, T.; Liu, Y. H.; Xue, J. S., Mechanisms for Lithium Insertion in Carbonaceous Materials. *Science* 1995, 270, 590-593.
10. Besenhard, J. O.; Yang, J.; Winter, M., Will advanced lithium-alloy anodes have a chance in lithium-ion batteries? *Journal of Power Sources* 1997, 68, 87-90.
11. Kasavajjula, U.; Wang, C. S.; Appleby, A. J., Nano- and bulk-silicon-based insertion anodes for lithium-ion secondary cells. *Journal of Power Sources* 2007, 163, 1003-1039.
12. Yu, C. J.; Li, X.; Ma, T.; Rong, J. P.; Zhang, R. J.; Shaffer, J.; An, Y. H.; Liu, Q.; Wei, B. Q.; Jiang, H. Q., Silicon Thin Films as Anodes for High-Performance Lithium-Ion Batteries with Effective Stress Relaxation. *Advanced Energy Materials* 2012, 2, 68-73.
13. Wu, H.; Cui, Y., Designing nanostructured Si anodes for high energy lithium ion batteries. *Nano Today* 2012, 7, 414-429.

14. Liu, X. H.; Zheng, H.; Zhong, L.; Huan, S.; Karki, K.; Zhang, L. Q.; Liu, Y.; Kushima, A.; Liang, W. T.; Wang, J. W.; Cho, J. H.; Epstein, E.; Dayeh, S. A.; Picraux, S. T.; Zhu, T.; Li, J.; Sullivan, J. P.; Cumings, J.; Wang, C. S.; Mao, S. X.; Ye, Z. Z.; Zhang, S. L.; Huang, J. Y., Anisotropic Swelling and Fracture of Silicon Nanowires during Lithiation. *Nano Letters* 2011, 11, 3312-3318.
15. Lee, S. W.; McDowell, M. T.; Choi, J. W.; Cui, Y., Anomalous Shape Changes of Silicon Nanopillars by Electrochemical Lithiation. *Nano Letters* 2011, 11, 3034-3039.
16. Lee, S. W.; McDowell, M. T.; Berla, L. A.; Nix, W. D.; Cui, Y., Fracture of crystalline silicon nanopillars during electrochemical lithium insertion. *P Natl Acad Sci USA* 2012, 109, 4080-4085.
17. Liu, X. H.; Zhong, L.; Huang, S.; Mao, S. X.; Zhu, T.; Huang, J. Y., Size-Dependent Fracture of Silicon Nanoparticles During Lithiation. *Acs Nano* 2012, 6, 1522-1531.
18. Yang, H.; Huang, S.; Huang, X.; Fan, F. F.; Liang, W. T.; Liu, X. H.; Chen, L. Q.; Huang, J. Y.; Li, J.; Zhu, T.; Zhang, S. L., Orientation-Dependent Interfacial Mobility Governs the Anisotropic Swelling in Lithiated Silicon Nanowires. *Nano Letters* 2012, 12, 1953-1958.
19. Liu, X. H.; Wang, J. W.; Huang, S.; Fan, F. F.; Huang, X.; Liu, Y.; Krylyuk, S.; Yoo, J.; Dayeh, S. A.; Davydov, A. V.; Mao, S. X.; Picraux, S. T.; Zhang, S. L.; Li, J.; Zhu, T.; Huang, J. Y., In situ atomic-scale imaging of electrochemical lithiation in silicon. *Nat Nanotechnol* 2012, 7, 749-756.
20. Cubuk, E. D.; Wang, W. L.; Zhao, K. J.; Vlassak, J. J.; Suo, Z. G.; Kaxiras, E., Morphological Evolution of Si Nanowires upon Lithiation: A First-Principles Multiscale Model. *Nano Letters* 2013, 13, 2011-2015.
21. Bower, A. F.; Guduru, P. R.; Sethuraman, V. A., A finite strain model of stress, diffusion, plastic flow, and electrochemical reactions in a lithium-ion half-cell. *Journal of the Mechanics and Physics of Solids* 2011, 59, 804-828.
22. Zhao, K. J.; Pharr, M.; Cai, S. Q.; Vlassak, J. J.; Suo, Z. G., Large Plastic Deformation in High-Capacity Lithium-Ion Batteries Caused by Charge and Discharge. *Journal of the American Ceramic Society* 2011, 94, S226-S235.
23. An, Y.; Jiang, H., A finite element simulation on transient large deformation and mass diffusion in electrodes for lithium ion batteries. *Model Simul Mater Sc* 2013, 21, 074007.
24. Cui, Z. W.; Gao, F.; Qu, J. M., Interface-reaction controlled diffusion in binary solids with applications to lithiation of silicon in lithium-ion batteries. *Journal of the Mechanics and Physics of Solids* 2013, 61, 293-310.
25. Schmalzried, H., *Chemical kinetics of solids*. VCH: Weinheim ; New York, 1995; p xvi, 433 p.
26. Laidler, K. J., *Chemical kinetics*. 3rd ed.; Harper & Row: New York, 1987; p xi, 531 p.
27. Chan, M. K. Y.; Wolverton, C.; Greeley, J. P., First Principles Simulations of the Electrochemical Lithiation and Delithiation of Faceted Crystalline Silicon. *Journal of the American Chemical Society* 2012, 134, 14362-14374.
28. Liu, X. H.; Fan, F. F.; Yang, H.; Zhang, S. L.; Huang, J. Y.; Zhu, T., Self-Limiting Lithiation in Silicon Nanowires. *Acs Nano* 2013, 7, 1495-1503.
29. Tritsarlis, G. A.; Zhao, K. J.; Okeke, O. U.; Kaxiras, E., Diffusion of Lithium in Bulk Amorphous Silicon: A Theoretical Study. *Journal of Physical Chemistry C* 2012, 116, 22212-22216.
30. Ding, N.; Xu, J.; Yao, Y. X.; Wegner, G.; Fang, X.; Chen, C. H.; Lieberwirth, I., Determination of the diffusion coefficient of lithium ions in nano-Si. *Solid State Ionics* 2009, 180, 222-225.
31. Haxhimali, T.; Karma, A.; Gonzales, F.; Rappaz, M., Orientation selection in dendritic evolution. *Nature Materials* 2006, 5, 660-664.
32. Qin, R. S.; Bhadeshia, H. K. D. H., Phase-field model study of the effect of interface anisotropy on the crystal morphological evolution of cubic metals. *Acta Mater* 2009, 57, 2210-2216.
33. Zheng, Q. S., Theory of Representations for Tensor Functions—A Unified Invariant Approach to Constitutive Equations. *Applied Mechanics Reviews* 1994, 47, 545-587.
34. Truesdell, C.; Noll, W., *The non-linear field theories of mechanics*. 2nd ed.; Springer-Verlag: Berlin ; New York, 1992; p x, 591 p.
35. Sethian, J. A., A review of level set and fast marching methods for image processing. *Modern Methods in Scientific Computing and Applications* 2002, 75, 365-396.

36. Boettinger, W. J.; Warren, J. A.; Beckermann, C.; Karma, A., Phase-field simulation of solidification. *Annual Review of Materials Research* 2002, 32, 163-194.
37. Tang, M.; Belak, J. F.; Dorr, M. R., Anisotropic Phase Boundary Morphology in Nanoscale Olivine Electrode Particles. *Journal of Physical Chemistry C* 2011, 115, 4922-4926.
38. Tang, M.; Huang, H. Y.; Meethong, N.; Kao, Y. H.; Carter, W. C.; Chiang, Y. M., Model for the Particle Size, Overpotential, and Strain Dependence of Phase Transition Pathways in Storage Electrodes: Application to Nanoscale Olivines. *Chemistry of Materials* 2009, 21, 1557-1571.
39. Chon, M. J.; Sethuraman, V. A.; McCormick, A.; Srinivasan, V.; Guduru, P. R., Real-Time Measurement of Stress and Damage Evolution during Initial Lithiation of Crystalline Silicon. *Physical Review Letters* 2011, 107, 045503.
40. Zhao, K. J.; Wang, W. L.; Gregoire, J.; Pharr, M.; Suo, Z. G.; Vlassak, J. J.; Kaxiras, E., Lithium-Assisted Plastic Deformation of Silicon Electrodes in Lithium-Ion Batteries: A First-Principles Theoretical Study. *Nano Letters* 2011, 11, 2962-2967.
41. Kushima, A.; Huang, J. Y.; Li, J., Quantitative Fracture Strength and Plasticity Measurements of Lithiated Silicon Nanowires by In Situ TEM Tensile Experiments. *Acs Nano* 2012, 6, 9425-9432.
42. Hopcroft, M. A.; Nix, W. D.; Kenny, T. W., What is the Young's Modulus of Silicon? *J Microelectromech S* 2010, 19, 229-238.
43. Hertzberg, B.; Benson, J.; Yushin, G., Ex-situ depth-sensing indentation measurements of electrochemically produced Si-Li alloy films. *Electrochemistry Communications* 2011, 13, 818-821.
44. McDowell, M. T.; Ryu, I.; Lee, S. W.; Wang, C. M.; Nix, W. D.; Cui, Y., Studying the Kinetics of Crystalline Silicon Nanoparticle Lithiation with In Situ Transmission Electron Microscopy. *Advanced Materials* 2012, 24, 6034-+.
45. Ye, J. C.; An, Y. H.; Heo, T. W.; Biener, M. M.; Nikolic, R. J.; Tang, M.; Jiang, H.; Wang, Y. M., Enhanced lithiation and fracture behavior of silicon mesoscale pillars via atomic layer coatings and geometry design. *Journal of Power Sources* 2014, 248, 447-456.
46. Kim, S. K.; Day, R. W.; Cahoon, J. F.; Kempa, T. J.; Song, K. D.; Park, H. G.; Lieber, C. M., Tuning Light Absorption in Core/Shell Silicon Nanowire Photovoltaic Devices through Morphological Design. *Nano Letters* 2012, 12, 4971-4976.
47. Seidel, H.; Csepregi, L.; Heuberger, A.; Baumgartel, H., ANISOTROPIC ETCHING OF CRYSTALLINE SILICON IN ALKALINE-SOLUTIONS .2. INFLUENCE OF DOPANTS. *Journal of the Electrochemical Society* 1990, 137, 3626-3632.
48. Seidel, H.; Csepregi, L.; Heuberger, A.; Baumgartel, H., ANISOTROPIC ETCHING OF CRYSTALLINE SILICON IN ALKALINE-SOLUTIONS .1. ORIENTATION DEPENDENCE AND BEHAVIOR OF PASSIVATION LAYERS. *Journal of the Electrochemical Society* 1990, 137, 3612-3626.
49. Huang, Z.; Geyer, N.; Werner, P.; de Boor, J.; Goesele, U., Metal-Assisted Chemical Etching of Silicon: A Review. *Advanced Materials* 2011, 23, 285-308.
50. Vanderbilt, D., Soft self-consistent pseudopotentials in a generalized eigenvalue formalism. *Phys Rev B* 1990, 41, 7892-7895.
51. Perdew, J. P.; Burke, K.; Ernzerhof, M., Generalized Gradient Approximation Made Simple. *Physical Review Letters* 1996, 77, 3865-3868.
52. Paolo, G.; Stefano, B.; Nicola, B.; Matteo, C.; Roberto, C.; Carlo, C.; Davide, C.; Guido, L. C.; Matteo, C.; Ismaila, D.; Andrea Dal, C.; Stefano de, G.; Stefano, F.; Guido, F.; Ralph, G.; Uwe, G.; Christos, G.; Anton, K.; Michele, L.; Layla, M.-S.; Nicola, M.; Francesco, M.; Riccardo, M.; Stefano, P.; Alfredo, P.; Lorenzo, P.; Carlo, S.; Sandro, S.; Gabriele, S.; Ari, P. S.; Alexander, S.; Paolo, U.; Renata, M. W., QUANTUM ESPRESSO: a modular and open-source software project for quantum simulations of materials. *Journal of Physics: Condensed Matter* 2009, 21, 395502.
53. Monkhorst, H. J.; Pack, J. D., Special points for Brillouin-zone integrations. *Phys Rev B* 1976, 13, 5188-5192.

Tables

Table 1. Miller index, directional vector, and values of invariants in representative directions

$\langle hkl \rangle$	$\langle 100 \rangle$	$\langle 110 \rangle$	$\langle 111 \rangle$	$\langle 112 \rangle$
(n_1, n_2, n_3)	$(1, 0, 0)$	$\left(\frac{1}{\sqrt{2}}, \frac{1}{\sqrt{2}}, 0\right)$	$\left(\frac{1}{\sqrt{3}}, \frac{1}{\sqrt{3}}, 1\right)$	$\left(\frac{1}{\sqrt{6}}, \frac{1}{\sqrt{6}}, \frac{2}{\sqrt{6}}\right)$
$I_1 = n_1^2 + n_2^2 + n_3^2$	1	1	1	1
$I_2 = n_1^2 n_2^2 + n_2^2 n_3^2 + n_3^2 n_1^2$	0	1/4	1/3	1/4
$I_3 = n_1^2 n_2^2 n_3^2$	0	0	1/27	1/54

Figures

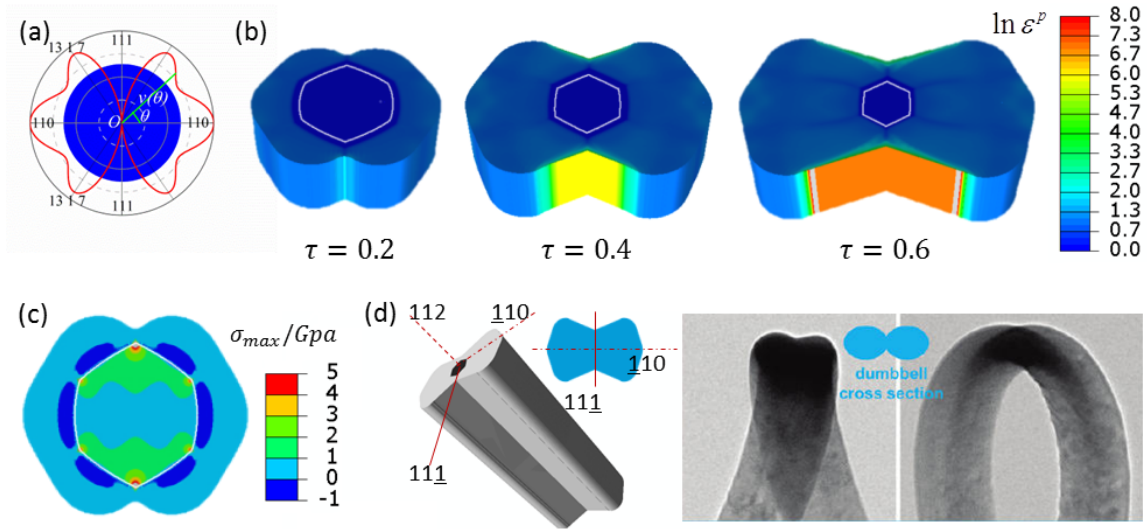


Figure 1. Lithiation of a $\langle 112 \rangle$ crystal nanowire with a circular cross-section. (a) Variation of the interface velocity $v(\theta)$ along different interface directions as a function of angle θ with respect to the $[110]$ crystal direction. The blue circle is the initial cross-section geometry. (b) Snapshots of nanowire morphologies, interface profiles (white solid line), and colormaps of equivalent plastic strain at different normalized lithiation times $\tau = 0.2, 0.4, 0.6$. (c) Colormap of maximum in-plane stress over the nanowire cross-section at time $\tau = 0.2$. (d) Comparison of the simulated morphology of a $\langle 112 \rangle$ nanowire (left panel) with TEM observations of anisotropic swelling of $\langle 112 \rangle$ nanowires in Reference [14] (right panel). The dumbbell cross-section is successfully captured by our simulation.

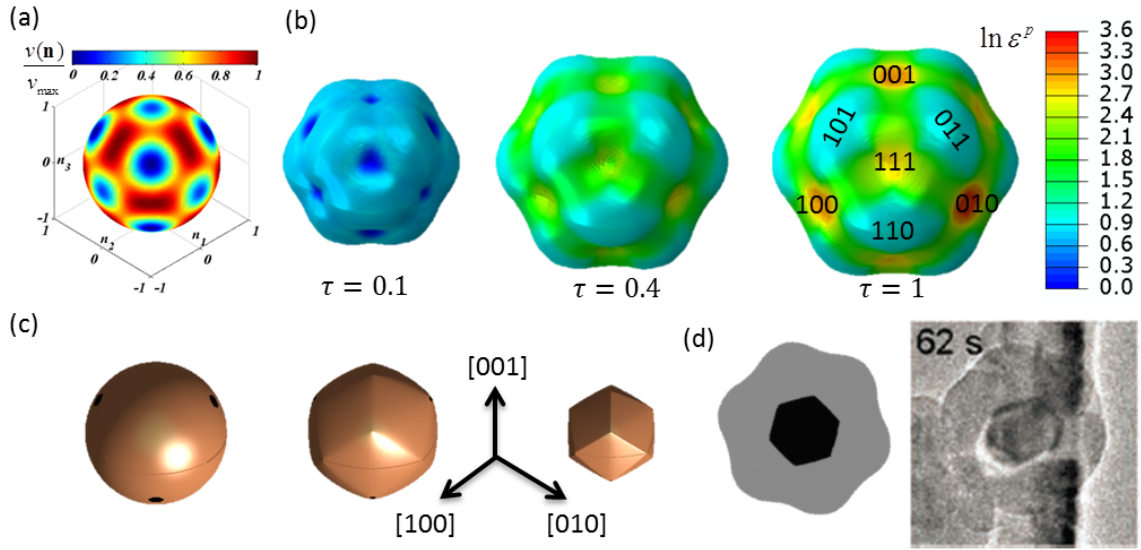


Figure 2. Lithiation of a 3D spherical crystal nanoparticle. (a) Variation of the interface velocity with spatial angle, colormapped on the surface of a unit sphere with the same spherical geometry as the initial crystal particle. (b) Colormaps of equivalent plastic strain on the deformed surface of the particle at different normalized lithiation times $\tau = 0.1, 0.4, 0.6$. (c) Morphologies of interfaces between amorphous shell and crystal core at different normalized lithiation times $\tau = 0, 0.1, 0.4$. The interface vanishes at time $\tau = 1$. (d) Comparison of the simulated morphology of the amorphous shell and crystal core at time $\tau = 0.4$, with a TEM image of a lithiated nanoparticle from Reference ???. Both profiles of the amorphous and crystal phases are well captured.

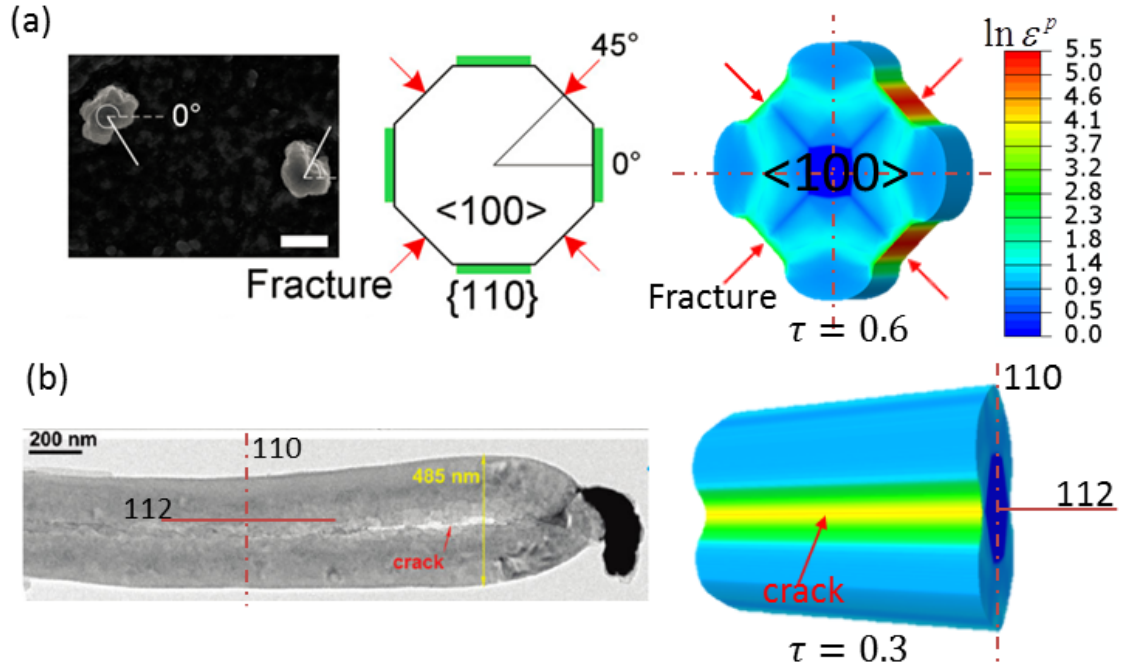


Figure 3. Comparison of the directional fracture behavior of (a) $\langle 100 \rangle$ and (b) $\langle 112 \rangle$ circular nanowires from experiments with simulation results. The nanowires fracture along planes bisecting two nearest in-plane $\langle 110 \rangle$ directions in experiments (left panels), which correspond to the directions for which the equivalent plastic strain concentration is highest in the simulations (right panels) at time (a) $\tau = 0.6$ and (b) $\tau = 0.3$. The correspondence suggests that the concentrated plastic strain on the surface accounts for the fracture of the circular nanowires.

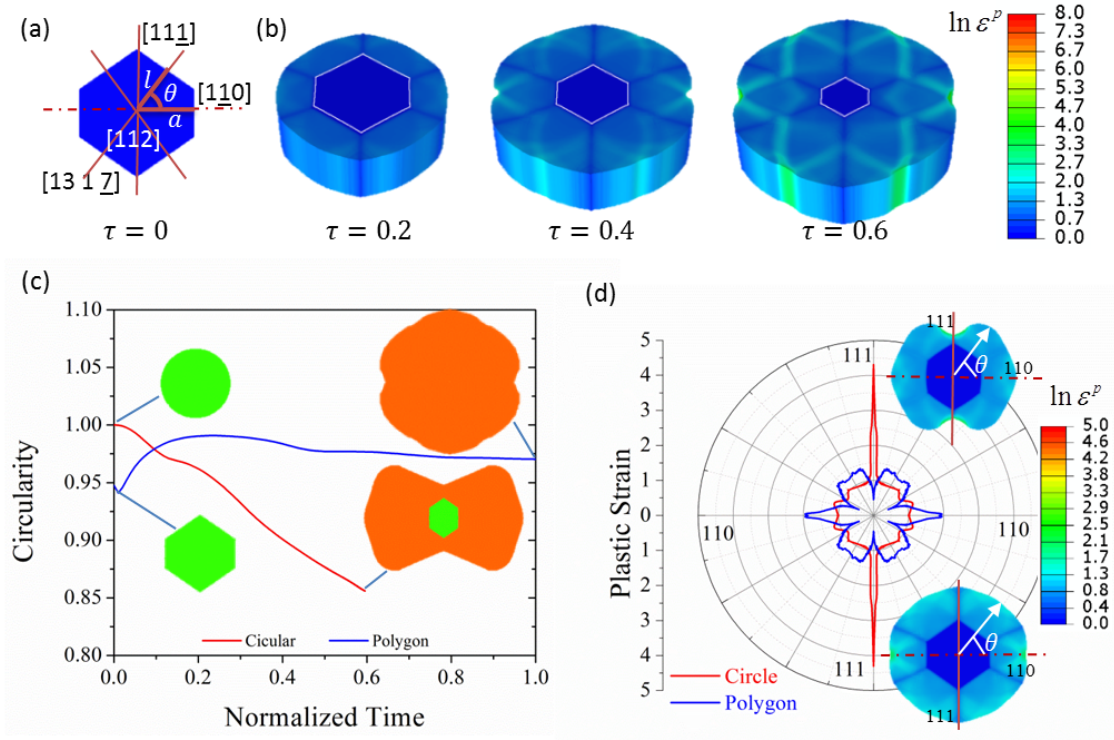


Figure 4. Lithiation of a $\langle 112 \rangle$ crystalline silicon nanowire with a polygon cross-section designed according to the rules in the text. (a) Initial polygon cross-section, for which angles and lengths marked in white satisfy $\theta=55^\circ$ and $l/a = 0.91$, as determined by the interface velocity profile in Fig. 1a. (b) Snapshots of nanowire morphologies, interface profiles (white solid line), and colormaps of equivalent plastic strain at different normalized lithiation times $\tau = 0.2, 0.4, 0.6$. (c) Comparison of the circularity of $\langle 112 \rangle$ nanowires with circular and polygon cross-sections as function of time, demonstrating that the polygon nanowire has a much more isotropic geometry after lithiation. (d) The equivalent plastic strain on the perimeter of circular and polygon cross-sections of $\langle 112 \rangle$ nanowires, plotted as a function of the angle from the in-plane $\langle 110 \rangle$ directions (marked in white) at time $\tau = 0.3$. The insets show the corresponding colormaps of equivalent plastic strain for the circular (top) and polygon (bottom) cross-sections, demonstrating that the polygon design helps to suppress the high concentration of plastic strain in certain directions.

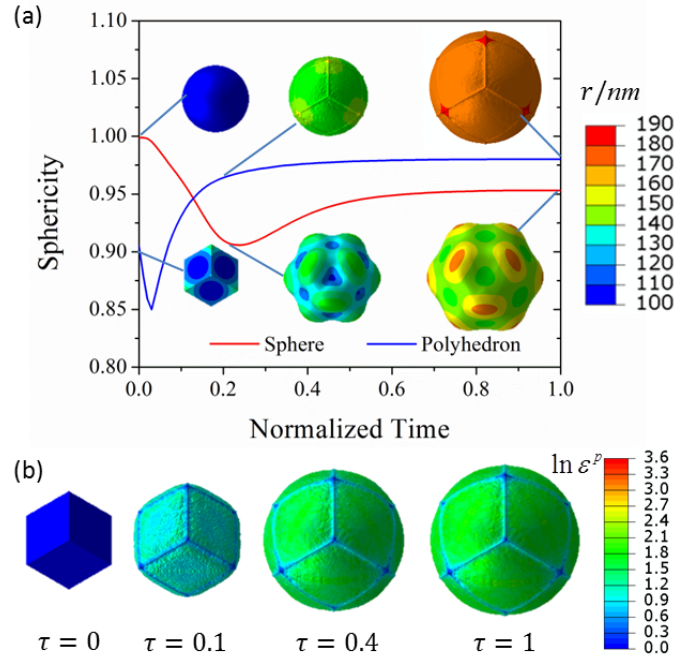


Figure 5. Lithiation of a 3D crystal nanoparticle with a rhombic dodecahedron geometry designed according to the rules in the text. (a) Comparison of the sphericity of nanoparticles with spherical or polyhedral initial shapes as function of time, demonstrating that the polyhedron nanoparticle has a much more isotropic morphology after lithiation. Insets are colormaps of distances between the deformed surface and the center of the particle at selected times. (b) Colormaps of equivalent plastic strain on the deformed surface of the particle at different normalized lithiation times $\tau = 0, 0.1, 0.4, 0.6$, with the $\tau = 0$ panel showing the original electrode geometry. Comparison with results for the spherical particle (Fig. 4b) shows that plastic strain is significantly reduced.

Support Information

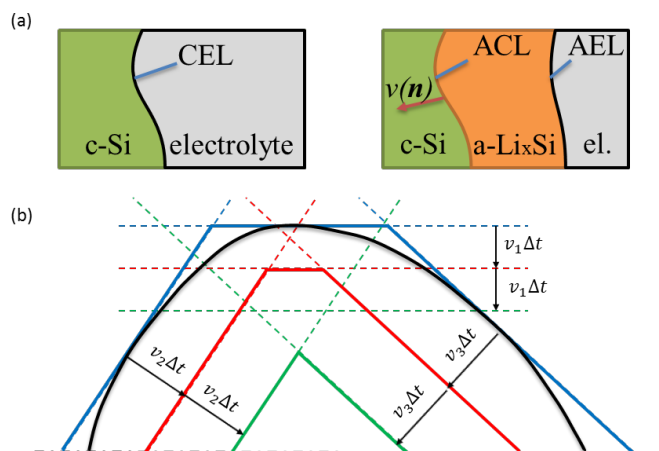


Figure S1. (a) Illustration of the first electrochemical lithiation of crystal silicon, showing definitions for CEI (crystalline-electrolyte interface), ACI (amorphous-crystalline interface), and AEI (amorphous-electrolyte interface); (b) Illustration of the algorithm to update the ACI position in our model. The initial ACI position (black solid line) is discretized by the smallest envelope (blue solid lines) formed by many tangent lines (blue dashed lines). As lithiation proceeds, the tangent lines move inwards step by step (red and green dashed lines), and the ACI position is updated (red and green solid lines on the smallest envelope).

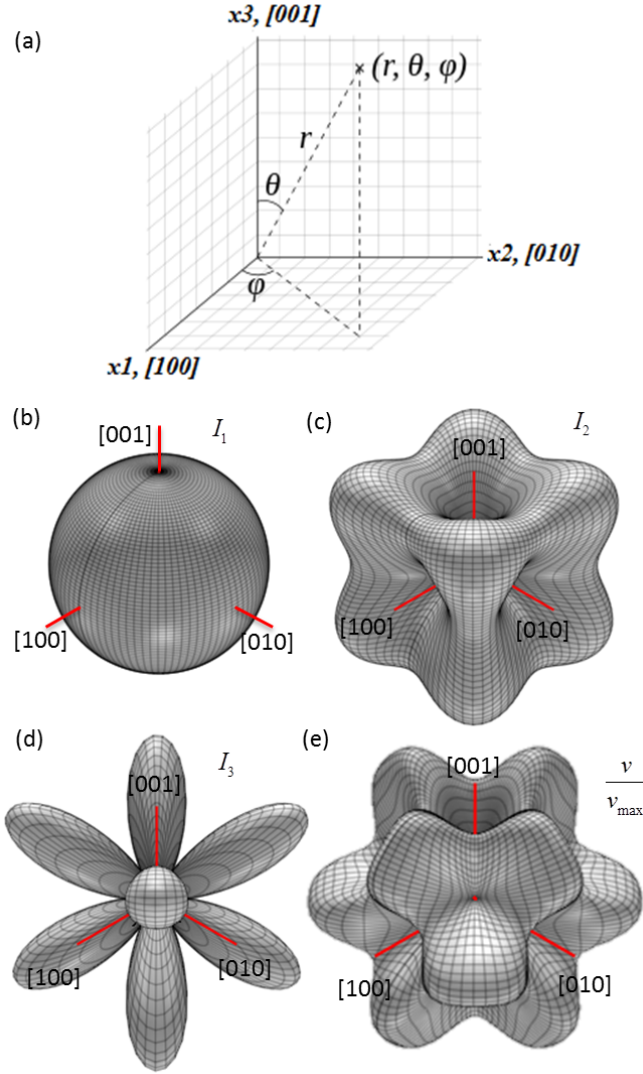


Figure S2. Surfaces defined in a spherical coordinate system (a) by (b) $r = I_1(\theta, \phi)$; (c) $r = I_2(\theta, \phi)$; (d) $r = I_3(\theta, \phi)$, showing the directional dependence of three invariants; (e) $r = v(\theta, \phi)/v_{\max}$, showing directional dependence of the ACI velocity for parameter $\eta = 1/6$.

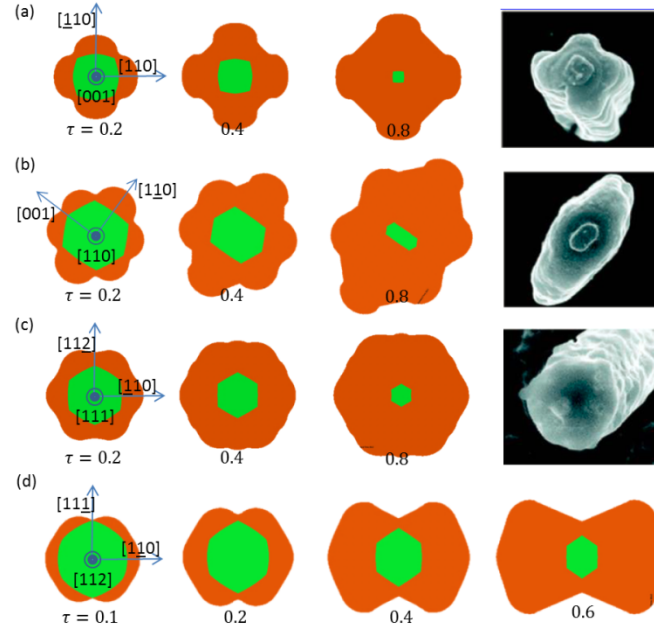


Figure S3. Anisotropic lithiation of a nanowire with four typical orientations. Snapshots of nanowire morphologies, interface profiles and phase transitions for (a) $\langle 100 \rangle$; (b) $\langle 110 \rangle$; (c) $\langle 111 \rangle$; (d) $\langle 112 \rangle$ wires at selected normalized lithiation times. Experimental observation of the anomalous shape change in silicon nanowires (last panel in (a-c)) are compared with simulations, showing that the shape changes for $\langle 100 \rangle$, $\langle 110 \rangle$, and $\langle 111 \rangle$ nanowires are reproduced.

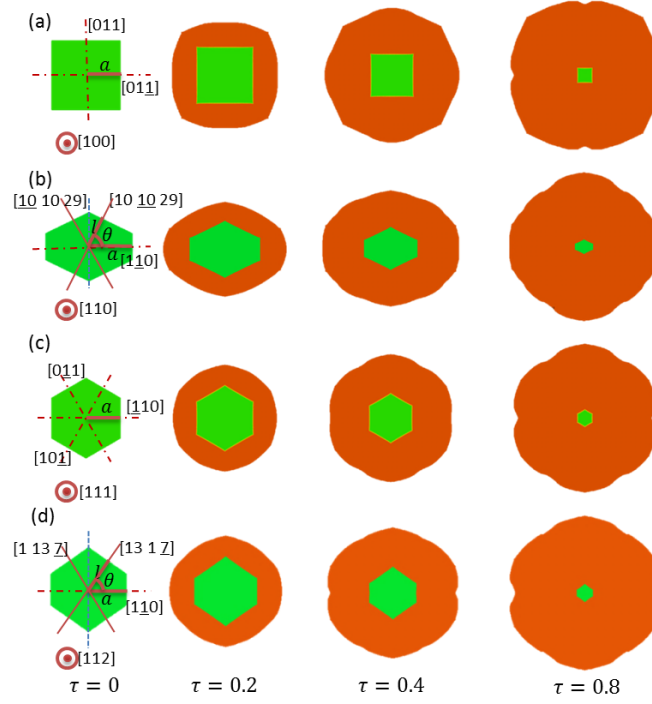


Figure S4. Optimal design of (a) $\langle 100 \rangle$ nanowire with a square cross-section; (b) $\langle 110 \rangle$ nanowire with a polygon cross-section ($\theta=64^\circ$ and $l/a = 0.72$); (c) $\langle 111 \rangle$ nanowire with a hexagonal cross-section; (d) $\langle 112 \rangle$ nanowire with a polygon cross-section ($\theta=55^\circ$ and $l/a = 0.91$). Snapshots of nanowire morphologies, interface profiles and phase transitions are shown at normalized lithiation times $\tau = 0.2, 0.4, 0.8$ for each of the nanowires, with the $\tau = 0$ panel showing the original geometry.

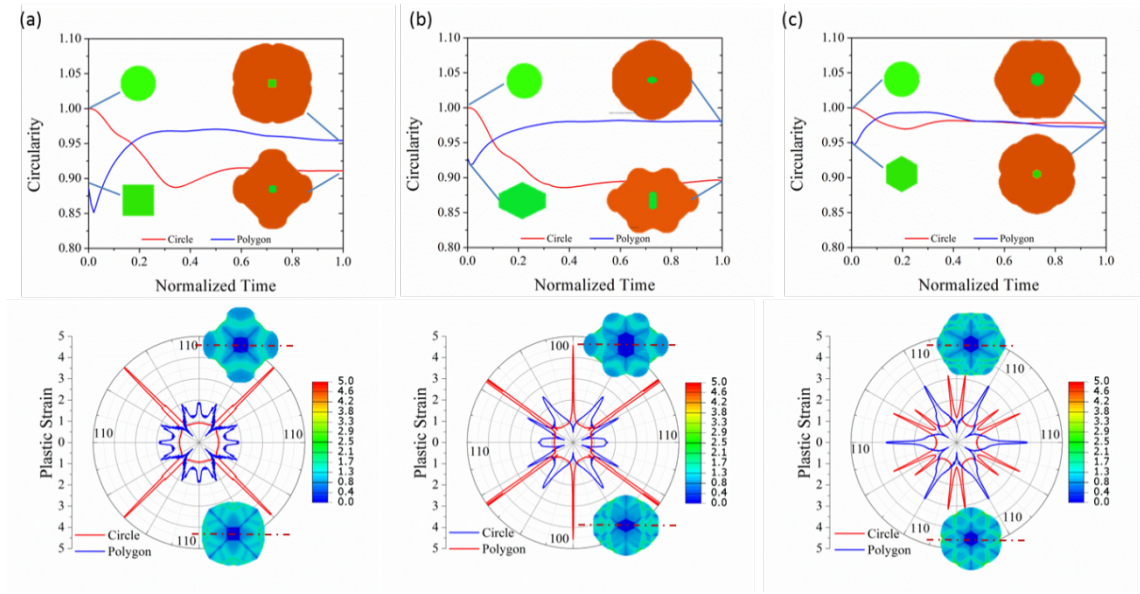


Figure S5. Comparison of the circularity as function of time (upper panel), and plastic strain on the perimeter of the cross-section as function of in-plane angle at time $\tau = 0.6$ (lower panel), for (a) $\langle 100 \rangle$; (b) $\langle 110 \rangle$; and (c) $\langle 112 \rangle$ nanowires with circular and polygon cross-sections. The specially designed polygon nanowires have much more isotropic geometries after lithiation, which helps to suppress the high concentration of plastic strain in certain directions. The benefits from adopting a polygon geometry for the $\langle 111 \rangle$ wire are marginal because the interface velocity in the cross-section is much less anisotropic.

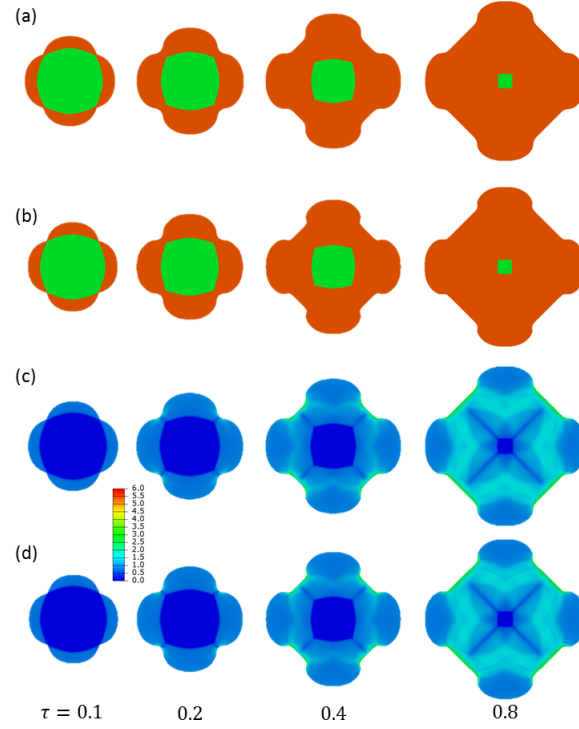


Figure S6. Phase evolution and equivalent plastic strain in <100> nanowire with circular cross-section for different η . (a-b) Phase evolution (amorphous in orange, crystal in green) for (a) $\eta = \frac{1}{6}$ and (b) for $\eta = 0$; (c-d) equivalent plastic strain for (c) $\eta = \frac{1}{6}$ and (d) for $\eta = 0$. Note that our simulation results are insensitive for relatively small values of η .

Description of method for estimation of η

In the main text, the parameter η is used to describe the relative velocity of the lithiation interface along $\langle 100 \rangle$ with respect to $\langle 110 \rangle$ and $\langle 111 \rangle$. As partial motivation for our choice of η and the ordering of the reaction front velocities, we performed density functional theory calculations of strain energy for thin surface slabs aligned along each of these directions. Each of the slabs was eight layers thick and carved from the corresponding bulk geometry with surface reconstruction and atomic relaxation disallowed. The system therefore simulates two surface-vacuum interfaces with four independent layers each; the thin slabs were deliberately chosen so as to ensure that the calculated strain energies are associated with surface rather than bulk character. To compute the strain energies, biaxial strain was applied within the surface plane only.

Periodic boundary conditions were applied, with 12 Å vacuum inserted perpendicular to the slab direction. An ultrasoft pseudopotential⁵⁰ with the Perdew-Burke-Ernzerhof (PBE) exchange-correlation functional⁵¹ was employed for Si, with plane wave and charge density cutoffs of 24 Ry and 240 Ry, respectively, as implemented in the Quantum ESPRESSO code⁵². A Monkhorst-Pack⁵³ \mathbf{k} -point mesh was used, based on a primitive-cell sampling of $(6 \times 6 \times 6)$ and scaled appropriate to the surface of interest.

The Li insertion barrier is expected to correlate with the strain energy associated with locally expanding the slab parallel to the surface, so as to accommodate the diffusing Li. However, because the surface boundary conditions are fixed by the underlying crystalline Si lattice immediately beyond the amorphous-crystalline interface, we assume that local expansion must be accompanied by secondary local lattice compression, such that the total area of the surface is conserved. Accordingly, we examine the surface slabs under both tensile and compressive strain.

The area-specific strain energy for the slabs is shown as a function of strain in [Fig. S7a](#). Note that the strain is defined relative to the equilibrium bulk lattice parameter, which does not necessarily correspond to the equilibrium lattice parameter of the surface slab due to intrinsic surface stress.

Accordingly, the (100) and (111) surfaces have intrinsic compressive surface stress (minimum strain energy occurs below the bulk equilibrium lattice spacing), whereas the (110) surface has weak intrinsic tensile surface stress. To estimate the total strain energy s introduced by straining the lattice to accommodate Li insertion, we average the area-normalized strain energy induced by tension with the equivalent quantity induced by compression, according to:

$$s = \frac{\Delta E^+ + \Delta E^-}{2A_0}$$

where ΔE^+ and ΔE^- are changes in total internal energy associated with the application of local tensile (+) and compressive (-) strain, and A_0 is the surface area of the slab at the equilibrium bulk lattice parameter. Note that this definition assumes the total surface area of the slab is conserved, as indicated above. As shown in Fig. S7b, the quantity s is smallest for the (110) plane and largest for the (111) plane, with the intermediate (100) result far closer to the (111) value than the (110) value. This means that the relative interface velocities of reaction fronts perpendicular to these planes, which are exponentially dependent on the insertion barriers via an Arrhenius relation, should have the ordering $\langle 110 \rangle \gg \langle 100 \rangle >$

$\langle 111 \rangle$. We can use our computed values of s to compute a composite strain ratio $r = \frac{s_{(111)} - s_{(100)}}{s_{(111)} - s_{(110)}}$, which

describes the relative insertion barrier along $\langle 100 \rangle$ with respect to $\langle 110 \rangle$ and $\langle 111 \rangle$ and is related to the choice of the parameter η . For non-negligible strains, the ratio r has an upper bound of ~ 0.4 , but decreases with increasing magnitude of the local surface strain induced upon Li insertion. In the immediate vicinity of Li, it is reasonable to assume that local areal strains greater than 10% may be observed, which lowers the expected value of r to less than 0.2. We conclude that η should have a very small value (i.e., $\ll 0.5$), justifying our choice of $1/6$. Notably, as we show for one example geometry in Figure S6, our conclusions do not change qualitatively if we set η to be even smaller (i.e., zero).

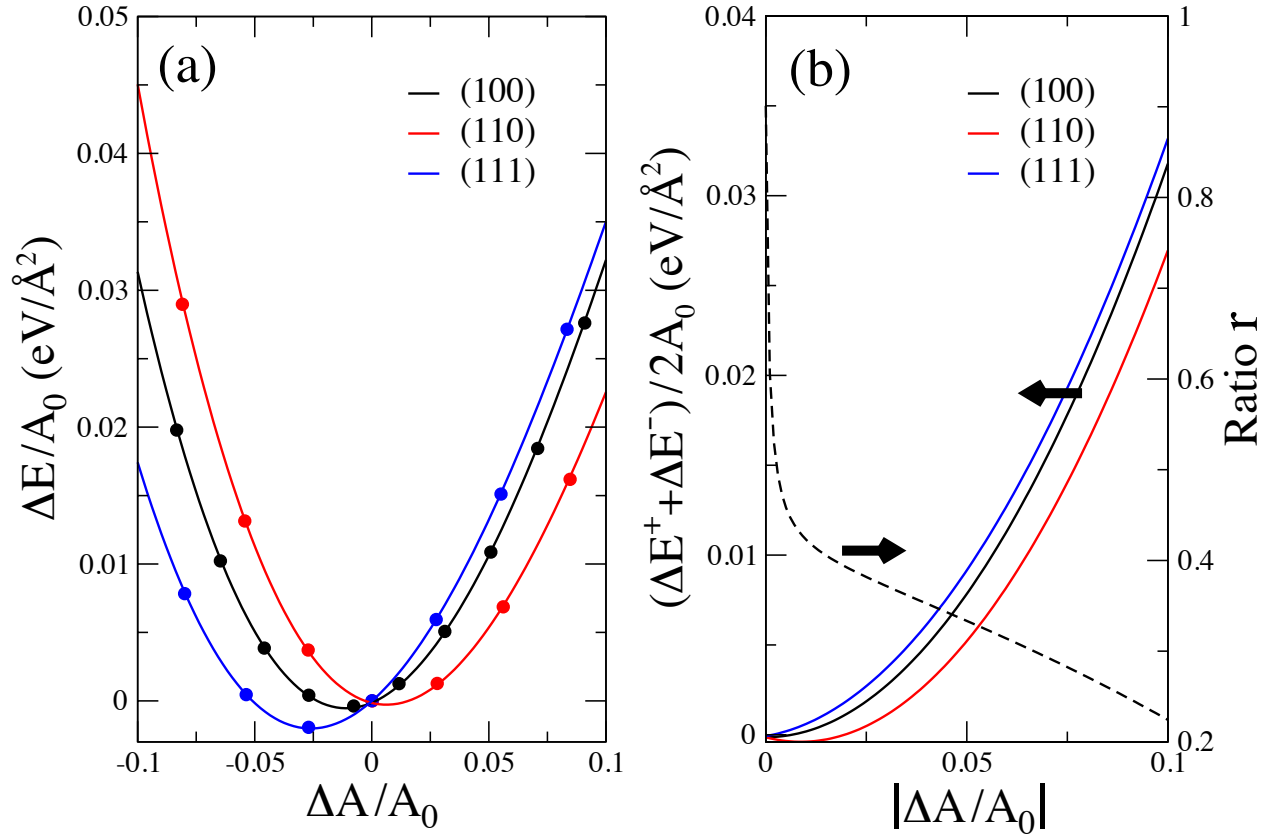


Figure S7. Procedure for estimating ordering of Li reaction front velocities based on strain induced in a Si surface slab upon lithiation, calculated using DFT. (a) Area-normalized strain energy $\Delta E / A_0$ for the (100), (110), and (111) surface slabs. Here, $\Delta A / A_0$ is the relative areal strain (negative/positive = compressive/tensile; the zero value represents the surface area at the equilibrium bulk lattice parameter), and ΔE is the associated change in total internal energy. (b) Left axis: Total area-normalized strain energy $s = (\Delta E^+ + \Delta E^-) / 2A_0$ as a function of local strain magnitude $|\Delta A / A_0|$, obtained by averaging the surface slab strain energy under local compressive strain and under tensile strain. Here, ΔE^+ and ΔE^- are changes in total internal energy associated with the application of tensile (+) and compressive (-) strain. Right axis: Value of the ratio r , defined as $r = \left(s_{(111)} - s_{(100)} \right) / \left(s_{(111)} - s_{(110)} \right)$.